

Spin structure of nanocrystalline terbiumJ. Weissmüller,^{1,2,*} A. Michels,^{1,2} D. Michels,² A. Wiedenmann,³ C. E. Krill III,² H. M. Sauer,² and R. Birringer²¹*Forschungszentrum Karlsruhe, Institut für Nanotechnologie, P.O. Box 3640, 7602 Karlsruhe, Germany*²*Universität des Saarlandes, Technische Physik, Saarbrücken, Germany*³*Hahn-Meitner Institut, BENSC, Berlin, Germany*

(Received 9 July 2003; revised manuscript received 10 November 2003; published 5 February 2004)

We present an experimental study of the magnetic microstructure in the nanocrystalline hard magnet Tb. Field-dependent small-angle neutron scattering (SANS) data are analyzed quantitatively in terms of the correlation function of the spin misalignment. We find that up to applied fields of several tesla the magnetization remains “locked in” to the basal planes of the hcp crystal lattice of each individual crystallite, but that the in-plane orientation of the spins is highly nonuniform within each grain. This spin disorder at the nanoscale can be suppressed by a large applied field, but in the remanent state the disorder reduces the magnetization to values considerably below the Stoner limit. In field-dependent SANS, the intragrain spin disorder gives rise to a crossover of the scattering curves, and to the unusual finding that the scattering cross section at small scattering vector increases with increasing magnetic field. As the origin of the internal spin disorder within the grains, we propose an extra magnetic anisotropy energy at small grain size, presumably due to microstrain, a suggestion which is supported by analysis of ac-susceptibility data in the paramagnetic state. Our finding of a reduced remanence at small grain size is contrary to the remanence enhancement that is observed in other nanocrystalline hard magnets. We also report an unusual logarithmic field dependence of the magnetization over wide ranges of the applied field and temperature.

DOI: 10.1103/PhysRevB.69.054402

PACS number(s): 75.50.Tt, 61.12.Ex, 75.50.Ww, 81.07.Bc

I. INTRODUCTION

In nanocrystalline (nc) ferromagnets the orientation of the magnetization vector is highly nonuniform on the nanometer scale, because at each grain boundary the set of crystallographic “easy axes” for the magnetization changes its orientation. Studying the detailed nature of this nonuniformity is of importance for understanding the macroscopic magnetic properties of nc materials. Several recent micromagnetics computer simulations explore the magnetic microstructure of nc hard magnets as a function of the grain size, of the anisotropy energy, and of the magnitude of the exchange coupling in the grain boundary regions,^{1–4} but there are practically no experimental data on the nanoscale magnetic microstructure in the bulk of these materials. This is a consequence of the inadequate lateral resolution of present microscopic techniques (Kerr, magnetic force, and Lorentz microscopy as well as scanning electron microscopy with polarization analysis) and of their inability to image the magnetic domain structure in the bulk, as opposed to at the surface. At present, the only known technique with a potential to resolve the magnetic microstructure in the bulk and on the length scale of nanometers is magnetic small-angle neutron scattering (SANS).

Studies of SANS in nominally saturated nanocrystalline soft^{5–8} and hard⁹ magnets have provided information on the nuclear microstructure. Investigations of the magnetic microstructure by SANS have been carried out on essentially soft magnetic nc samples of the elemental transition metals Fe, Ni, and Co,^{10–15} and on nc soft magnets crystallized from glasses.¹⁶ It has recently become possible to analyze such data quantitatively by employing a model for magnetic SANS by ferromagnets which is applicable near saturation. This approach supplies quantitative data on the magnetic mi-

crostructure, the exchange-stiffness constant, the magnitude and microstructure of the magnetic anisotropy,^{13,14,17} and the magnetostatic stray field.¹⁸ Similar to the computer models applied to hard magnets, the magnetic SANS analysis is based on the theory of micromagnetics. This continuum theory describes the variation of the orientation of the magnetization as a function of position and time based on a balance of the torques on the magnetic moments due to the anisotropy, the applied and demagnetizing fields, and the exchange interaction.

The magnetic microstructure of nc hard magnets, unlike that of soft magnets, has not been studied by SANS so far. In this paper, we present such a study, an investigation of the nc rare earth Tb. Single crystal Tb is ferromagnetic below 220 K;¹⁹ an intermediate antiferromagnetic phase with a helical spin structure and a periodicity of 9–10 lattice constants along the *c* axis of the hexagonal lattice²⁰ is stable up to the Néel temperature of 229 K. Tb has an extraordinarily large magnetocrystalline anisotropy. It not only confines the moments to the basal plane of the hcp lattice under most experimental conditions in the ferromagnetic regime, but it results also in a significantly anisotropic susceptibility even in the paramagnetic state. As the basal planes of neighboring crystals in a polycrystal are not coplanar, the large anisotropy imposes, depending on the crystallographic misorientation between neighboring grains, a variation of the spin orientation from grain to grain. The present study aims at investigating the nature of this highly perturbed spin structure in the nc material and of its dependence on the magnetic field.

The first part of this paper (Sec. II) discusses the theory of SANS by hard magnets, with emphasis on two issues, the separation of magnetic from nuclear scattering, and the analysis of the scattering data in terms of real-space information. Frequently, the separation of nuclear and magnetic scat-

tering is based on the assumption that the first is isotropic whereas the second varies with the angle ϑ between the applied magnetic field \mathbf{H}_a and the scattering vector \mathbf{q} as $\sin^2 \vartheta$.⁵ This is adequate when the scattering is due to jumps in the magnitude of the magnetization in a saturated magnetic material, for instance at the boundaries between magnetic particles and a nonmagnetic matrix. However, in single-phase bulk ferromagnets the magnetic scattering arises from the misalignment of the magnetic moments; near saturation the scattering will then vary as $(1 + \cos^2 \vartheta)$, whereas both magnitude and angular variation of the scattering in the demagnetized state and at intermediate fields depend strongly on the field and on the nature of the magnetic interaction.^{14,17} This precludes the application of the $\sin^2 \vartheta$ law to determine the nuclear scattering. It has been found that even in soft magnetic materials the scattering from the spin misalignment is not entirely suppressed by the magnetic fields which are typically available from electromagnets (≤ 2 T). Nevertheless, the nuclear scattering cross section can be determined by a suitable extrapolation to the idealized saturated state, based on field-dependent SANS data recorded in the approach-to-saturation regime.^{14,17} Because of their large magnetic anisotropy, hard magnets require a considerably larger field for saturation. In fact, the material of the present work could not be saturated with the available magnetic field, and as a consequence the extrapolation method was inapplicable. However, we could make use of the fact that the Curie temperature T_C of Tb is below room temperature, so that the material can be studied in the paramagnetic state above T_C , without incurring the risk of irreversible coarsening of the microstructure by grain growth. Section II A shows how the combined nuclear and magnetic scattering due to pores and second phases in the ferromagnetic state can be determined from scattering data for the material in the paramagnetic state.

The question of how information on the real-space spin structure can be extracted from experimental spin-misalignment scattering cross sections is the subject of debate. Some authors maintain that a characteristic size of coherently magnetized regions can be evaluated by decomposing the scattering into contributions from hypothetical hard spheres with a distribution of sizes.^{10,21} However, concerns were raised on the grounds that models for the magnetic microstructure suggest continuous variations of the spin-misalignment angle with a wide spectrum of wavelengths, very much unlike the homogeneously magnetized domains with sharp boundaries which are implied by the hard sphere analysis.²² The continuous variation of the spin orientation is indeed well known for ferromagnetic amorphous alloys. The elastic magnetic differential scattering cross section of these materials can be modeled by a Lorentzian-squared term, which arises from an exponential decay in the correlation of the spin orientation, with a well-defined correlation length.²³ This exponential decay has a firm foundation in the random magnetic anisotropy theory for the magnetism of amorphous materials. In the absence of an equivalent model for nanocrystalline hard magnets, we find it desirable to use a model-independent approach in analyzing the scattering data. This is further supported by the

observation that the magnetic scattering of nanocrystalline ferromagnets will frequently display power laws steeper than q^{-4} , which cannot be reproduced by hard-sphere models or by the Lorentzian-squared terms.¹⁴ In Sec. II C of this paper we show how quantitative information on the magnetic microstructure can be derived from SANS data if a model-independent analysis of the (auto)correlation function of the spin-misalignment angle is carried out.

Sections III and IV present experimental procedures and results, respectively, both for the magnetic and structural characterization and for SANS. One of the intriguing experimental findings is that the magnetic SANS at small scattering vector \mathbf{q} increases with increasing applied magnetic field H_a . This is contrary to the case of soft magnets, and it contradicts the common trend that the progressive ordering of the spin system by increasing H_a will necessarily decrease the scattering contrast arising from the spin misalignment. In Sec. V we discuss the results, and we present a model that can qualitatively explain the experimental observation.

II. THEORY

A. Elastic magnetic SANS

The elastic differential scattering cross section $d\Sigma/d\Omega$ for SANS (assuming a nonpolarized incident beam and neglecting spin-dependent nuclear scattering) at scattering vector \mathbf{q} due to atoms at positions \mathbf{x}_j is given by^{14,24}

$$\frac{d\Sigma}{d\Omega}(\mathbf{q}) = \frac{1}{V} \sum_{j,l} (b_{\text{nuc},j} b_{\text{nuc},l} + b_{\text{mag},j} b_{\text{mag},l} \mathbf{Q}_j \cdot \mathbf{Q}_l) \times \exp[i\mathbf{q}(\mathbf{x}_j - \mathbf{x}_l)], \quad (1)$$

where b_{nuc} and b_{mag} denote the atomic nuclear and magnetic scattering lengths, respectively, V is the volume, and \mathbf{Q} represents the Halpern-Johnson vector, which is related to a unit vector $\boldsymbol{\varepsilon}$ in the direction of \mathbf{q} and to the atomic magnetic moment $\boldsymbol{\mu}_a$, by the vector function $\mathbf{Q} = \boldsymbol{\varepsilon}(\boldsymbol{\varepsilon} \cdot \boldsymbol{\mu}_a / \mu_a) - \boldsymbol{\mu}_a / \mu_a$.^{25,26}

Equation (1) accounts for scattering due to variations in the atomic density and composition and to variations in the magnitude and orientation of the magnetic moment. Of interest for studies of the magnetic microstructure are the variations of the orientation of the magnetic moment, and it is therefore desirable to separate this “spin-misalignment scattering” from scattering due to the nonuniform atomic density and to the ensuing variations of the local magnitude of the magnetization. We have previously discussed this separation for the case of a multicomponent material in the limit where the angle of misalignment of the magnetic moments relative to the field direction is small.¹⁴ For hard magnets the misalignment angle will not generally be small since the large anisotropy will tilt the spins even at large applied magnetic fields. This prevents the application of our previous results to hard magnets, but a formal separation of the spin misalignment scattering is still possible if attention is restricted to single-component ferromagnets with uniform magnitude of μ_a and of b_{mag} . To this end, the atomic magnetic moments vectors $\boldsymbol{\mu}_{a_j}$ are decomposed into the mean

value over all atoms, $\langle \boldsymbol{\mu}_a \rangle$, and the difference vector, $\Delta \boldsymbol{\mu}_{a,j} = \boldsymbol{\mu}_{a,j} - \langle \boldsymbol{\mu} \rangle$. The Halpen-Johnson vectors \mathbf{Q}_j are decomposed analogously, so that $\mathbf{Q}_j = \langle \mathbf{Q} \rangle + \Delta \mathbf{Q}_j$ and

$$\langle \mathbf{Q} \rangle = \boldsymbol{\varepsilon} \left(\boldsymbol{\varepsilon} \cdot \frac{\langle \boldsymbol{\mu}_a \rangle}{\mu_a} \right) - \frac{\langle \boldsymbol{\mu}_a \rangle}{\mu_a} \quad (2)$$

can be substituted in Eq. (1). We use the angular brackets $\langle \rangle$ to denote averages throughout this paper. By definition, the mean value of $\Delta \mathbf{Q}$ vanishes, and the contributions of the terms $b_{\text{mag}}^2 \Delta \mathbf{Q}_j \langle \mathbf{Q} \rangle$ to the sum in Eq. (1) will therefore cancel. The remaining terms can be grouped into the two additive scattering cross sections $d\Sigma_R/d\Omega$ and $d\Sigma_M/d\Omega$, the first containing only terms b_{nuc} and $b_{\text{mag}} \langle \mathbf{Q} \rangle$, and the second only terms $b_{\text{mag}} \Delta \mathbf{Q}$:

$$\begin{aligned} \frac{d\Sigma_R}{d\Omega}(\mathbf{q}) &= \frac{N}{V} \frac{\sigma_{\text{inc}}}{4\pi} + \frac{1}{V} \left[\langle b_{\text{nuc}} \rangle^2 + b_{\text{mag}}^2 \frac{\langle \mu_a \rangle^2}{\mu_a^2} \sin^2 \vartheta \right] \\ &\times \left| \sum_j \exp(i\mathbf{q}\mathbf{x}_j) \right|^2 \end{aligned} \quad (3)$$

$$\frac{d\Sigma_M}{d\Omega}(\mathbf{q}) = \frac{1}{V} b_{\text{mag}}^2 \left| \sum_j \Delta \mathbf{Q}_j \exp(i\mathbf{q}\mathbf{x}_j) \right|^2. \quad (4)$$

The symbol σ_{inc} denotes the nuclear incoherent scattering. By inspection of Eq. (3) it is seen that the ‘‘residual scattering cross section’’ Σ_R depends on the nuclear microstructure through the nuclear interference function,

$$P_{\text{nuc}}(\mathbf{q}) = \frac{1}{N} \left| \sum_j \exp(i\mathbf{q}\mathbf{x}_j) \right|^2, \quad (5)$$

where N denotes the number of atoms, and through a prefactor which varies as a function of the vector mean of the magnetic moment. Σ_R depends only on the nuclear microstructure and on the mean magnetization, and is otherwise independent of the magnetic microstructure. The scattering due to the nonuniform orientation of the magnetization, that is, due to the magnetic microstructure, is isolated in the cross section for ‘‘spin-misalignment scattering’’ Σ_M .

The macroscopic mean magnetization $\langle \mathbf{M} \rangle$, which can be measured with a magnetometer, scales with the mean atomic moment. This allows one to estimate $\langle \boldsymbol{\mu}_a \rangle$ in Eq. (3) from experimental magnetization data according to

$$\frac{\langle \boldsymbol{\mu}_a \rangle}{\mu_a} = \frac{\langle \mathbf{M} \rangle}{M_S}, \quad (6)$$

where M_S denotes the saturation magnetization.

For small-angle scattering the discreteness of the atomic structure of matter is of no importance, so that the sum in Eq. (4) can, quite analogously to the usual procedure in nuclear small-angle scattering, be replaced by an integral based on the continuous function $\Delta \mathbf{Q}(\mathbf{x}) = \boldsymbol{\varepsilon}(\boldsymbol{\varepsilon} \cdot \mathbf{M}_P(\mathbf{x})/M_S) - \mathbf{M}_P(\mathbf{x})/M_S$. \mathbf{M}_P is defined as the difference between the local magnetization and the macroscopic mean magnetization, $\mathbf{M}_P(\mathbf{x}) = \mathbf{M}(\mathbf{x}) - \langle \mathbf{M} \rangle$. The magnetic scattering cross section can then be expressed as

$$\frac{d\Sigma_M}{d\Omega}(\mathbf{q}) = \frac{8\pi^3}{V} b_{\text{mag}}^2 \rho_a^2 |\mathbf{m}(\mathbf{q})|^2 \sin^2 \alpha, \quad (7)$$

where \mathbf{m} denotes the Fourier transform of the reduced magnetization $\mathbf{M}_P(\mathbf{x})/M_S$,

$$\mathbf{M}_P(\mathbf{x})/M_S = (2\pi)^{-3/2} \int \int \int \mathbf{m}(\mathbf{q}) \exp(-i\mathbf{q}\mathbf{x}) d^3\mathbf{q}, \quad (8)$$

and α represents the angle included by \mathbf{m} and \mathbf{q} . In experimental SANS studies the scattering is measured only for \mathbf{q} in the plane normal to the incident neutron beam. Often it is useful to discuss a ‘‘radial average’’ differential cross section, averaged over all orientations of \mathbf{q} within this plane. For use in the next section we present results for this average in two situations of high symmetry: (i) the demagnetized texture-free soft magnet at vanishing applied fields and (ii) the nearly saturated texture-free ferromagnet. In (i), the vector \mathbf{m} takes on all orientations with equal probability and independent of the orientation of \mathbf{q} , whereas in (ii) the vectors \mathbf{M}_P and, therefore, \mathbf{m} are confined to the plane normal to $\langle \mathbf{M} \rangle$, with a constant expectation value independent of the orientation of \mathbf{q} . In both cases the expectation value of $|\mathbf{m}|$ is independent of the orientation of \mathbf{q} , so that $|\mathbf{m}(\mathbf{q})|^2 = m^2(q)$ and

$$\frac{d\bar{\Sigma}_M}{d\Omega}(q) = \frac{8\pi^3}{V} b_{\text{mag}}^2 \rho_a^2 m^2(q) \langle \sin^2 \alpha \rangle, \quad (9)$$

where the average $\langle \sin^2 \alpha \rangle$ takes on the values 2/3 and 3/4 in cases (i) and (ii), respectively.

The spin-misalignment scattering cross section Σ_M in the ferromagnetic state is due to the *static* magnetic microstructure; by contrast, in the paramagnetic state the magnetic scattering arises from thermally activated *dynamic* fluctuations of the spin direction. The cross section for the paramagnetic scattering is given by²⁷

$$\frac{d\Sigma_P}{d\Omega} = \frac{N}{V} \frac{2}{3} (\gamma_n r_0)^2 J(J+1), \quad (10)$$

where r_0 denotes the classical radius of the electron ($r_0 = 2.818 \times 10^{-15}$ m), γ_n is the neutron magnetic moment measured in units of nuclear magnetons ($\gamma_n = -1.913$), and J is the effective spin quantum number. In writing Eq. (10) we have omitted the atomic form factor, which is unity in the small-angle region.

By making use of Eq. (10) and of tabulated values for σ_{inc} and J , it is possible to determine the nuclear interference function for residual scattering from the experimental total scattering cross section in the paramagnetic state,

$$\frac{d\Sigma}{d\Omega}(\mathbf{q}) = \frac{N}{V} \frac{\sigma_{\text{inc}}}{4\pi} + \frac{d\Sigma_P}{d\Omega} + \frac{N}{V} \langle b_{\text{nuc}} \rangle^2 P_{\text{nuc}}(\mathbf{q}). \quad (11)$$

Once $P_{\text{nuc}}(\mathbf{q})$ is known the spin-misalignment scattering can be separated from the residual scattering by using the expression for scattering in the ferromagnetic state, obtained by combining Eqs. (3)–(5),

$$\frac{d\bar{\Sigma}}{d\Omega}(\mathbf{q}) = \frac{N}{V} \frac{\sigma_{\text{inc}}}{4\pi} + \frac{N}{V} \left[\langle b_{\text{nuc}} \rangle^2 + b_{\text{mag}}^2 \frac{\langle \mu_a \rangle^2}{\mu_a^2} \sin^2 \vartheta \right] P_{\text{nuc}}(\mathbf{q}) + \frac{d\bar{\Sigma}_M}{d\Omega}(\mathbf{q}). \quad (12)$$

For Tb, the nuclear scattering length is $b_{\text{nuc}} = 7.34 \times 10^{-15}$ m.²⁸ With the atomic moment $\mu_a = 9.34\mu_B$,³⁷ one obtains for the magnetic scattering length $b_{\text{mag}} = 0.27 \times 10^{-14}$ m $\times \mu_a / \mu_B = 25.2 \times 10^{-15}$ m. Since b_{mag} is significantly larger than b_{nuc} , the residual scattering cross section is dominantly magnetic.

B. Inelastic magnetic SANS

Since our interest is in the static magnetic microstructure, which is probed by elastic scattering, it is required to verify that the inelastic scattering cross section in the ferromagnetic state is negligible. We have previously shown¹⁴ that, for the spin-wave dispersion relation $\hbar\omega = Dq^2 + g\mu_B\mu_0H$ where $\hbar\omega$ and D denote the spin-wave energy and the spin-wave stiffness constant, respectively, the requirements of conservation of momentum and energy upon absorption or emission of a magnon cannot be satisfied simultaneously for any scattering vector in the small-angle regime when the field exceeds the critical value

$$H^* \approx \frac{\hbar^4 k_0^2}{4m^2 g \mu_0 \mu_B D} \quad (13)$$

(m , g , and k_0 denote, respectively, the neutron mass, the g factor, and the incident neutron wave vector). For $H \geq H^*$ the magnetic SANS is entirely elastic, as is required for analyzing the data in terms of our model. In materials with a large magnetocrystalline anisotropy, such as Tb, the spin-wave dispersion relation contains, as an extra term, the gap energy Δ . The computation of the critical field is readily generalized for the simplest such dispersion relation, $\hbar\omega = \Delta + Dq^2 + g\mu_B\mu_0H$. Since Δ and $g\mu_B\mu_0H$ are additive, Eq. (13) and its derivation will remain valid if H is consistently replaced by $H + \Delta/(g\mu_B\mu_0)$. The expression for the critical field will then take on the new form

$$H^* \approx \frac{\hbar^4 k_0^2}{4m^2 g \mu_0 \mu_B D} - \frac{\Delta}{g \mu_0 \mu_B}. \quad (14)$$

When the second term on the right-hand side is larger in magnitude than the first, then spin-wave scattering in the small-angle regime is suppressed at *any* field and wave vector.

We have estimated mean values of the exchange-stiffness constant A and of the spin-wave stiffness constant D in Tb from the interplanar exchange parameters,²⁹ using Eq. (3.20a) in Ref. 30 and averaging over the in-plane and out-of-plane interactions. This yields $A \approx 2.3 \times 10^{-11}$ J/m and $D \approx 150$ meV \AA^2 , so that the numerical value of the first term on the right in Eq. (14) for the critical field to suppress spin-wave scattering is about 0.4 T. Using the experimental values for the gap energy at the temperatures of our experiment, $\Delta/k_B = 20$ K at $T = 5$ K and $\Delta/k_B = 2 \pm 1$ K at $T = 200$ K,³¹

the magnitude of the second term is estimated at about 20 T at 5 K and 2 ± 1 T at 200 K. In spite of the uncertainty involved in the simplified representation of the dispersion relation, the implication of the large gap energy is therefore clearly that the critical field is negative, in other words, inelastic scattering is suppressed at all applied fields, so that the magnetic SANS signal is entirely elastic.

C. Correlation function and characteristic length

A (self-)correlation function $C(\mathbf{r})$ of the spin misalignment can be defined by

$$C(\mathbf{r}) = M_S^{-2} V^{-1} \int \int \int \mathbf{M}_P(\mathbf{x}) \cdot \mathbf{M}_P(\mathbf{x} + \mathbf{r}) d^3\mathbf{x}; \quad (15)$$

it is related to the Fourier transform \mathbf{m} of \mathbf{M}_P/M_S by

$$C(\mathbf{r}) = V^{-1} \int \int \int |\mathbf{m}(\mathbf{q})|^2 \exp(i\mathbf{q}\mathbf{r}) d^3\mathbf{q}. \quad (16)$$

By comparison to Eq. (7) it is seen that $|\mathbf{m}(\mathbf{q})|^2$ can be determined from the spin-misalignment scattering provided that the angles α are known. A rigorous evaluation of $C(\mathbf{r})$ may therefore require a knowledge of the complete information on the orientation and magnitude of the vector \mathbf{m} as a function of the orientation and magnitude of the wave vector \mathbf{q} . In general, the required database will not be available, but useful information on $C(\mathbf{r})$ can still be derived from experimental scattering cross sections. As above we consider the two limiting cases: (i) the isotropic (demagnetized) case, and (ii) the case of a nearly saturated texture-free ferromagnet. In both cases C is isotropic, $C = C(r)$, and

$$C(r) = \frac{1}{V} \int_{q=0}^{\infty} m^2(q) \frac{\sin(qr)}{qr} 4\pi q^2 dq. \quad (17)$$

By solving Eq. (9) for $m^2(q)$ and substituting the result into Eq. (17), we obtain

$$C(r) = a(2\pi^2 b_{\text{mag}}^2 \rho_a^2 r)^{-1} \int_{q=0}^{\infty} q \frac{d\bar{\Sigma}_M}{d\Omega}(q) \sin(qr) dq, \quad (18)$$

where $a = 1/\langle \sin^2 \alpha \rangle$ takes on the values 3/2 and 4/3 for cases (i) and (ii), respectively. In spite of the quite different orientation distributions of \mathbf{m} , these results agree to within better than $\pm 7\%$. In our data analysis we used the mean of both values, $a = 17/12 \approx 1.42$.

A characteristic length l_C of the spin misalignment can be defined in terms of the limit of the logarithmic derivative of $C(r)$ for $r \rightarrow 0$:

$$l_C = - \left(\frac{d \ln(C)}{dr} \right)^{-1} \Big|_{r \rightarrow 0}. \quad (19)$$

When fluctuations in the spin misalignment decay exponentially, the definition is then consistent with $C(r) \propto \exp(-r/l_C)$. Furthermore, in a granular system with discontinuous interfaces the correlation function of the grains is³²

$$C(r) \propto 1 - \frac{A}{4V_g} r \quad (20)$$

in the limit $r \ll R$ with R the radius of mean curvature of the interfaces. A and V_g denote the total surface or interface area and the total volume of the grains. This is readily seen to give $l_c = 4V_g/A$ and, for the special case of spherical particles, $l_c = 4R/3$. The result for spheres is confirmed by applying Eq. (19) to the known correlation function for the sphere,³³ $C(r) = 1 - 3r/(4R) + r^3/(16R^3)$ for $r \leq 2R$ and $C(r) = 0$ for $r > 2R$.

In addition to the characteristic length l_c , the analysis of $C(r)$ can also supply information on the mean magnetization. This is readily seen by considering Eq. (15) for $r=0$:

$$C(0) = \frac{1}{V} \int \int \int \frac{|\mathbf{M}_p(\mathbf{x})|^2}{M_S^2} d^3\mathbf{x} = \frac{\langle |\mathbf{M}_p|^2 \rangle}{M_S^2}. \quad (21)$$

In polar coordinates, and for uniform M_S , we can write $\mathbf{M}_p = M_S \{\sin \phi \sin \theta, \cos \phi \sin \theta, \cos \theta - \langle \cos \theta \rangle\}$, with θ the angle included by $\mathbf{M}(\mathbf{x})$ and $\langle \mathbf{M} \rangle$. It is then readily seen that $|\mathbf{M}_p|^2 = M_S^2 (1 - 2 \cos \theta \langle \cos \theta \rangle + \langle \cos \theta \rangle^2)$ and, since $|\langle \mathbf{M} \rangle| = M_S \langle \cos \theta \rangle$, that consequently $\langle |\mathbf{M}_p|^2 \rangle = M_S^2 - \langle \mathbf{M} \rangle^2$. This leads to the result

$$C(0) = 1 - \left(\frac{\langle \mathbf{M} \rangle}{M_S} \right)^2, \quad (22)$$

which links the correlation function to the macroscopic magnetization $\langle \mathbf{M} \rangle$.

It is well known that the lateral resolution and the size of the largest structure resolved in a small-angle scattering experiment depend, via the sampling theorem, on the upper and lower experimental scattering vector, respectively. In evaluating the integral Eq. (18) for experimental data limited to the interval $[q_{\min}, q_{\max}]$ one can obtain meaningful information on $C(r)$ only for distances r in the interval $[r_{\min}, r_{\max}]$ with, roughly, $r_{\min} = 2\pi/q_{\max}$ and $r_{\max} = \pi/q_{\min}$. In our experiments on Tb (see below), we used $q_{\min} = 0.06 \text{ nm}^{-1}$, $q_{\max} = 3 \text{ nm}^{-1}$, and consequently $r_{\min} = 2 \text{ nm}$, $r_{\max} = 50 \text{ nm}$. Besides limiting the resolution for the characteristic length, the finiteness of the experimental data also implies that the reduction of the mean magnetization, relative to M_S , that can be inferred from $C(0)$, is representative only for the effect of structure in the magnetization on scales between r_{\min} and r_{\max} . In particular, the results of SANS are insensitive to the macroscopic domain structure of a material.

III. EXPERIMENT AND DATA REDUCTION

Nanocrystalline Tb was prepared by the inert-gas condensation technique. The material was thermally evaporated in a 10^{-8} mbar base-pressure vacuum system, backfilled with a stationary He atmosphere of 10 mbar, using Al_2O_3 crucibles heated by tungsten foils. The powder was collected and consolidated *in situ* under high vacuum and at ambient temperature; pressure and duration were 1 GPa and 20 min, respectively. The samples are disks of diameter 8 mm and thickness of about 0.2 mm. Measurement by the Archimedes method indicated a mass density of $95 \pm 3\%$ of the literature value

for the coarse-grained material. Magnetic measurements were performed on rectangular rods, of dimension $0.2 \times 0.4 \times 6 \text{ mm}^3$, cut from the sample after completion of the SANS experiment. A coarse-grained reference sample for the magnetization measurements was obtained by annealing one of the rods for 10 min at 600°C in a vacuum of 5×10^{-6} mbar. Macroscopic magnetization isotherms were measured with a vibrating sample magnetometer (Oxford Instruments), and the magnetic susceptibility was determined with an ac susceptometer (Quantum Design PPMS). The demagnetization factors were estimated from the values for spheroids with aspect ratios similar to the samples. X-ray diffraction on the as-prepared samples was performed in Bragg-Brentano geometry using $\text{Mo } K\alpha_{1/2}$ radiation and a solid state detector.

The SANS experiments were carried out at instrument V4 at the Berlin Neutron Scattering Center (BENS). An unpolarized beam of wavelength $\lambda = 0.6 \text{ nm}$ and a wavelength spread $\Delta\lambda/\lambda = 0.15$ was used. The instrument was equipped with a 5 T vertical field cryomagnet with an estimated remanent field of 1 mT, and the sample was mounted on a 6 mm diameter Cd aperture. All SANS measurements were carried out with the sample first taken to the maximum field and the data then recorded at subsequently lower experimental fields. The series of measurements with various magnetic fields were repeated at each of three different sample-to-detector distances, covering a q range of about 0.06 to 3 nm^{-1} . The data were corrected in the usual way for absorption, detector efficiency, and background, and were converted to absolute units with the aid of a water standard. Care was taken to correct for the comparatively strong scattering by the entrance and exit windows of the cryostat. The sample transmission was measured for each field, and was found to vary only insignificantly when the field was increased from 1 mT to 4.5 T, from 0.65 to 0.69 at 5 K and from 0.79 to 0.73 at 200 K.

IV. EXPERIMENTAL RESULTS

A. X-ray diffraction

Figure 1(a) displays the x-ray diffraction pattern for the nc Tb sample. A mean grain size was determined by analysis of the integral breadth of the Bragg reflections, correcting for instrumental broadening and separating size- and strain-induced broadening by the method of Klug and Alexander assuming Cauchy size and Gaussian strain broadening.³⁴ The result for the grain size is $9.3 \pm 1.8 \text{ nm}$. Owing to the reflection overlap, the scatter in the results for the peak widths is considerable. As a consequence, only an upper limit for the root-mean square (rms) microstrain $\langle \varepsilon^2 \rangle^{1/2}$ was obtained, $\langle \varepsilon^2 \rangle^{1/2} < 0.6\%$.

The three reflections in the triplet around 15° scattering angle have similar widths, a finding that is contrary to results for nanocrystalline hcp Co, where a broad $\langle 101 \rangle$ reflection indicates a large number of stacking faults.¹⁴ The absence of this broadening in nc Tb indicates that faulting is insignificant. The ratio of the integrated intensities of the $\langle 100 \rangle$, $\langle 002 \rangle$, and $\langle 200 \rangle$ peaks is close to that of untextured powder samples, suggesting that the crystal orientations are random.

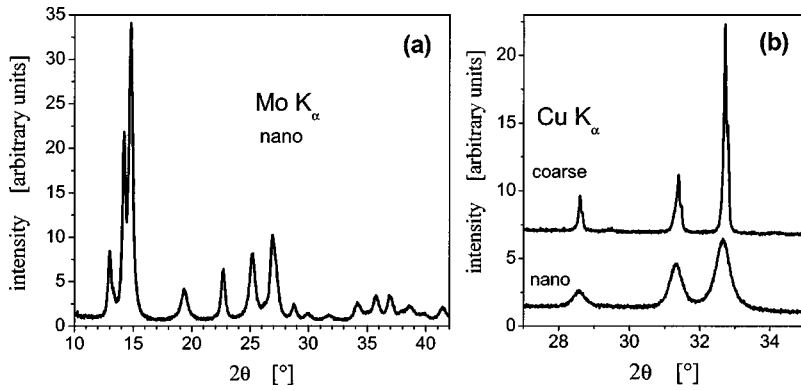


FIG. 1. X-ray diffraction intensity versus scattering angle 2θ for nanocrystalline (nc) and coarse-grained (cg) Tb. (a) Disk-shaped as-prepared sample used for SANS measured with Mo $K\alpha$ radiation. (b) Thin bar samples used for magnetometry measured with Cu $K\alpha$ radiation.

Because of the small sample volume the coarse-grained annealed sample (cg Tb) yielded only a weak scattering signal, which precluded an investigation in focusing diffraction geometry over a wide range of scattering vector. Instead, the scattering in the region of the most intense peaks was investigated with a position-sensitive detector and Ni-filtered Cu $K\alpha$ radiation, as displayed in Fig. 1(b). It was found that after the annealing the reflection width corresponds to the instrumental width; this indicates grain growth to a size of 100 nm or above.

B. ac susceptibility

Figure 2(a) displays the real part χ' of the ac susceptibility, measured at frequency 1000 Hz and amplitude 10 Oe, versus temperature T for the nanocrystalline and the coarse-grained samples. The most obvious result is that χ is considerably smaller for nc than for cg Tb, both in the ferromagnetic and in the paramagnetic state. Both curves exhibit maxima at about the same magnetic transition temperature. For cg Tb this corresponds to a ferromagnet-antiferromagnet transition, with a maximum χ at about $T_C=219$ K; this is in reasonable agreement with single-crystal data ($T_C=220$ K).¹⁹ The susceptibility of cg Tb exhibits a second narrow peak at the Néel temperature $T_N=229$ K. This transition is suppressed in the nc material in favor of a single maximum in χ at the Curie temperature of 224 K, significantly higher than T_C in the coarse-grained material. In contrast to this observation, a pronounced decrease in T_C at small grain size has been reported for nc Gd.³⁵

The broad “hump” in χ around $T=150$ K in cg Tb corresponds to a similar feature in single-crystal Tb, which has been attributed to changes in the relaxation dynamics;³⁶ this hump is absent in nc Tb.

The temperature dependence of the inverse paramagnetic susceptibility χ^{-1} is displayed in Fig. 2(b). According to the Curie-Weiss law for the mass susceptibility,

$$\chi = \frac{N_A \mu_a^2}{3m_a k_B (T - \theta_p)} \quad (23)$$

(where N_A is Avogadro’s number and m_a denotes the atomic weight), the paramagnetic atomic moment μ_a can be deduced from the slope of straight-line fits to $\chi^{-1}(T)$, while the abscissa intercept of the line indicates the paramagnetic Curie temperature θ_p . For cg Tb we obtain $\mu_a=9.75\mu_B$ and $\theta_p=231$ K, which is well compatible with the values for single-crystal Tb, $\mu_a=9.77\mu_B$ and $\theta_p=239$ and 195 K for H along the a and c axes of the hcp lattice, respectively.³⁷

The paramagnetic magnetization of an idealized, texture-free polycrystal is obtained by relating the magnetization to the field in terms of the susceptibility tensor of the single crystal, and taking the orientation average in crystal coordinates. For Tb the result is $\mathbf{M}=(2\chi_a/3+\chi_c/3)\mathbf{H}$ with χ_a and χ_c the susceptibilities along the a and c axes, respectively. When this expression is evaluated with Eq. (23) and the literature data for μ_a and for θ_p in the respective crystallographic direction, then a curved graph of χ^{-1} versus T is obtained; this can be readily understood as a consequence of the fact that, as the temperature approaches the ordering tran-

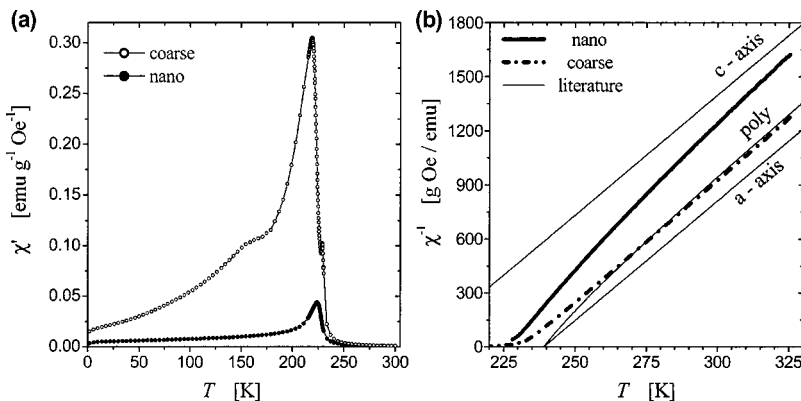


FIG. 2. (a) Experimental ac susceptibility χ' versus temperature T for nanocrystalline and coarse-grained Tb. (b) Inverse ac susceptibility χ^{-1} versus T for nanocrystalline (bold solid line) and coarse-grained (bold dash-dotted line) Tb. Thin solid lines: literature data (Ref. 39) for single-crystal Tb with the field oriented along the crystallographic a and c axes as indicated in the figure. Thin solid line marked “poly” refers to the inverse susceptibility of a texture-free coarse-grained polycrystal, computed by taking the orientation average of the single-crystal data for χ' in crystal coordinates.

sition from above, the diverging susceptibility of the crystallites with the highest θ_p will make an increasingly dominant contribution to the net susceptibility. The orientation-averaged susceptibility is plotted as one of the thin solid lines in Fig. 2(b); it is seen to agree quantitatively with the experimental data for cg Tb at temperatures sufficiently above θ_p . The fact that this good agreement to literature data was obtained with annealed nc Tb suggests that the magnetic properties are not noticeably affected by impurities, and that the modified magnetic properties in the nanocrystalline state, to be discussed below, are an intrinsic effect of the small size, not extrinsic due to impurities or second phases. In this context it is noted that the samples retained a shiny metallic surface even after exposure to air for about one year, and that they showed no detectable change in the magnetic properties over a period of several months. This is in contrast to inert-gas condensed transition metals, such as Fe, which pick up prohibitive amounts of oxygen upon exposure to air.³⁸

As compared to the data for cg Tb, the susceptibility of nc Tb is significantly lower at all temperatures, and the curvature in the plot of χ^{-1} versus T in the paramagnetic state is increased. Accurate estimates of μ_a are complicated by the significant curvature of $\chi^{-1}(T)$, but the graph of $\chi^{-1}(T)$ exhibits a tendency to align in parallel with that of cg Tb and with the single-crystal curves as T is increased. This trend could not be explored to arbitrarily high T , since the maximum temperature for experiment was limited by the need to prevent grain growth. We carried out repetitive measurements of $\chi(T)$; these gave identical results, indicating the absence of irreversible changes in the microstructure during heating to 325 K. A lower bound for the moment was obtained from the slope of $\chi^{-1}(T)$ at the highest temperature. In the interval 320–325 K the slope is 13.9 ± 0.4 (g Oe/emul)/K, which yields a paramagnetic moment of $(9.56 \pm 0.14)\mu_B$, within 2% of the single-crystal value. This suggests that the reduction of the grain size does not affect the mean atomic moment; in other words, there is no evidence for a significant reduction of μ_a at grain boundaries.

C. Magnetization

Figure 3 displays hysteresis loops at the temperature $T = 1.6$ K for cg and nc Tb. The most obvious finding is that nc Tb has a considerably larger coercivity than cg Tb, and a significantly lower magnetization at all fields. It is also found that, even at an applied field of $\mu_0 H_a = 12$ T, the magnetization of both materials falls significantly short of the saturation magnetization of single-crystal Tb, $\sigma_M = 328$ A m²/kg.³⁷ Also shown is the predicted remanent magnetization of texture-free polycrystalline Tb if the magnetization is locked in with the easy axis closest to the direction of the saturating field; this is the Stoner-Wohlfarth limit for the remanence,³⁹ which is more familiar in conjunction with isolated small particles, but which provides an equally adequate description of some bulk hard magnets.^{2,40} For a hexagonal crystal structure with six easy axes in the basal plane the theoretical remanent magnetization obtained in this way⁴¹ is $\frac{3}{4}M_S$, as

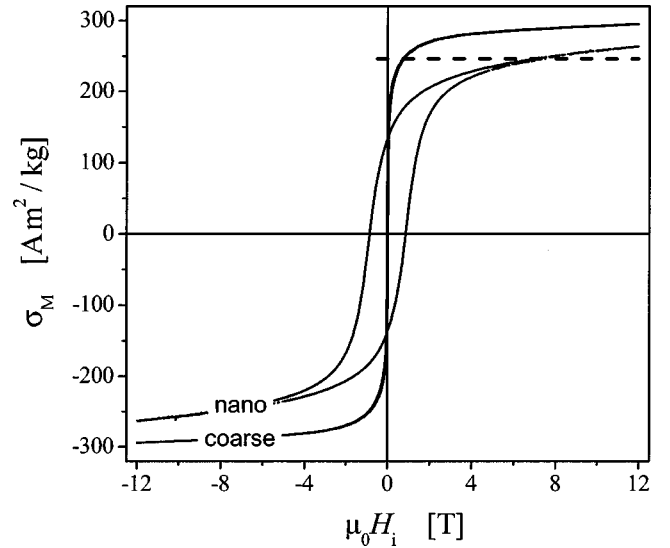


FIG. 3. Isotherms of the mass magnetization σ_M versus the internal field H_i at temperature $T = 1.6$ K for nanocrystalline and coarse-grained Tb (solid lines). Dashed line: Stoner-Wohlfarth limit for the remanence.

indicated by the dashed line in Fig. 3. It is seen that for applied fields below about 0.7 T for cg Tb, and below about 7 T for nc Tb, the magnetization of the samples is below the Stoner-Wohlfarth limit for the remanence; the reduced remanence for nc Tb at 1.6 K is $0.4M_S$.

A conceivable reason for the low apparent remanence is the occurrence of domains, magnetized at an angle to the applied field, in the region of demagnetizing fields near the edges of the rod-shaped samples. The effect of these fields is not adequately corrected for by subtraction of a uniform demagnetizing field. Since cg Tb has a low coercivity, it is conceivable that the local demagnetizing field may be sufficiently strong to nucleate such domains. However, since both samples have identical shape and dimension, and since nc Tb has a large coercivity which cannot be overcome by the demagnetizing field at edges, the reduced remanent magnetization in the nanoscale material, relative to cg Tb, cannot be explained in this way. This suggests the nanoscale grain size as the relevant factor.

The significant reduction of the magnetization at small grain size persists throughout the entire temperature interval up to $T = 300$ K, as can be seen in the overview plots of magnetization isotherms for the two samples below and above T_C (see Fig. 4). The magnetization isotherms at the Curie temperature and in the paramagnetic state confirm the smaller susceptibility of the nc material, which was already apparent from the ac susceptibility data.

It would be of interest to estimate the spontaneous magnetization or the saturation magnetization by extrapolation of the data. Satisfactory agreement with the high-field branches of the experimental loops are achieved by fits with the approach-to-saturation law $\sigma_M = \sigma_0 - a/\sqrt{H} - b/H - c/H^2 + dH$,³⁰ or with combinations of fewer elements of the series. However, the fit parameters a, b, c, d , and in particular the saturation magnetization σ_0 , vary strongly as a function of the choice of the interval in H which is considered in the fit.

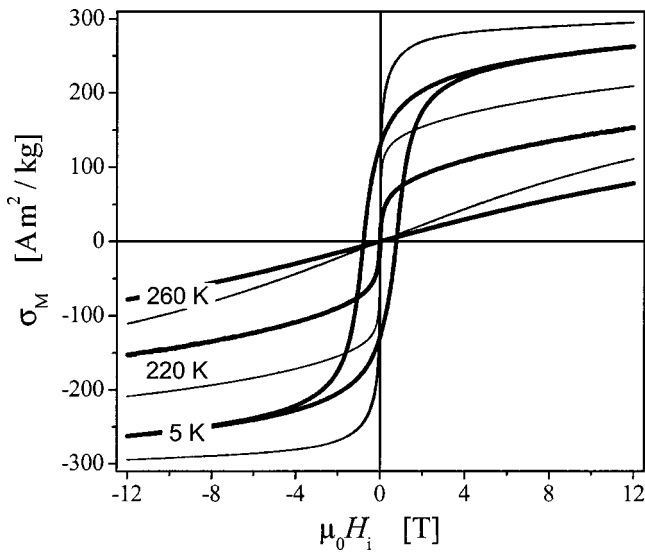


FIG. 4. Isotherms of the mass magnetization σ_M versus the internal field H_i at various temperatures as indicated in the figure. Bold lines, nc Tb; thin lines, cg Tb.

This indicates that, at the highest experimental field, the sample is too far from saturation to allow a reliable extrapolation. It may also be questioned whether the models underlying the asymptotic approach to saturation law apply to states this far from saturation.

Remarkably, it is found that, at low T , the magnetization of nc Tb can be quite accurately described as being proportional to the logarithm of the internal field, as can be seen in

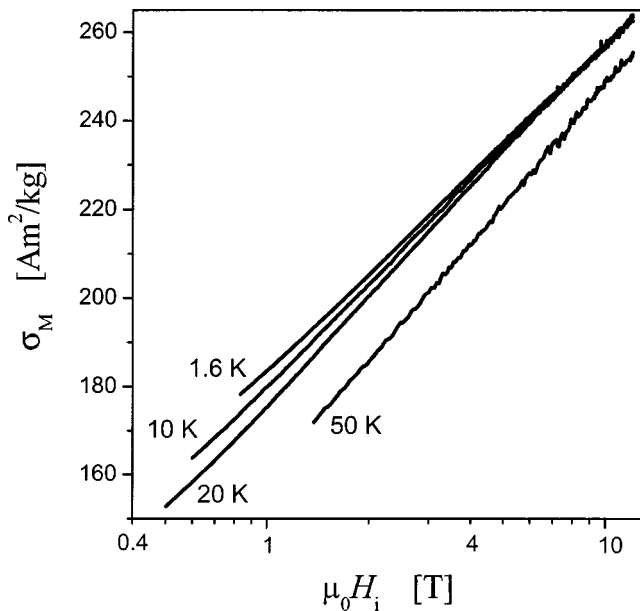


FIG. 5. Log-linear plot of the mass magnetization, recorded while decreasing the field, versus the internal magnetic field H_i for nc Tb. The temperature is indicated in the figure. Data are shown only in the interval where the relative deviation from a straight line is $\Delta\sigma_M/\sigma_M \leq 0.005$. The linear dependency indicates $\sigma_M \propto \log(H_i)$, which precludes estimating the spontaneous or saturation magnetization by extrapolation to $H_i=0$ or ∞ , respectively.

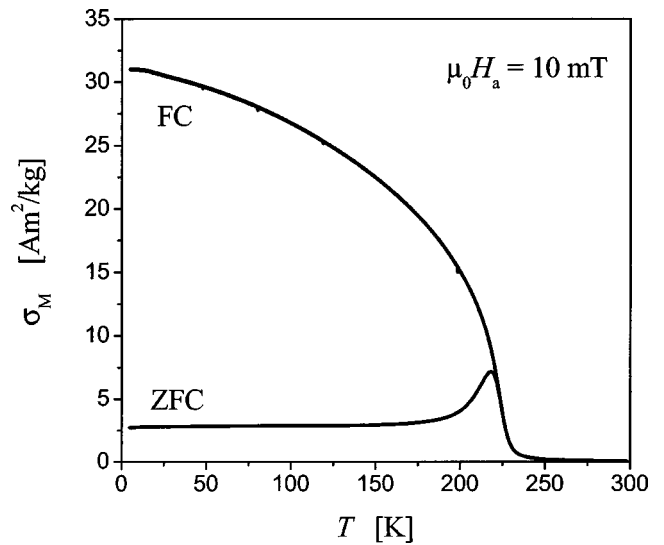


FIG. 6. Mass magnetization σ_M versus temperature T for nc Tb, measured upon heating at an applied field $\mu_0 H_a = 10$ mT after cooling with (FC) and without (ZFC) applied field.

Fig. 5. Over more than one decade of H_i , the data can be fitted by a straight line in the plot of σ_M versus $\log H_i$ when a maximum value of 0.005 for the relative deviation between data and fit is admitted. The divergence of the logarithm prevents a meaningful extrapolation of the data to $H_i=0$ or to $H_i=\infty$. We are unaware of a possible explanation for the origin of the logarithmic magnetization isotherm in terms of magnetic interactions in the nanocrystalline hard magnet.

Figure 6 shows data for the mass magnetization σ_M versus temperature T for nc Tb, measured upon heating at an applied field $\mu_0 H = 10$ mT after cooling with (FC) and without (ZFC) applied field. The ZFC magnetization exhibits a Hopkinson-like peak at the temperature where the coercivity becomes comparable to the applied field. There are no further prominent features in the plot, yet another indication that the sample does not contain second phases with different ordering temperatures.

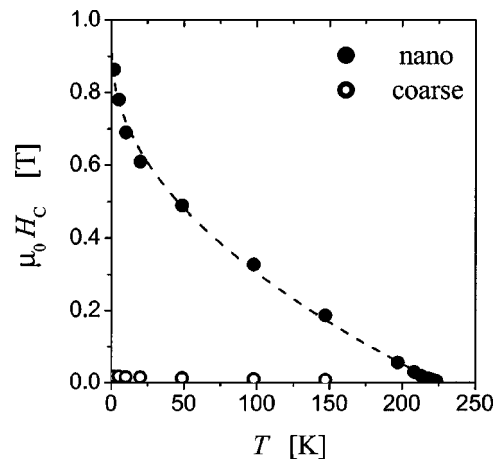


FIG. 7. Coercive field H_C versus temperature T for nanocrystalline (nc) and coarse-grained (cg) Tb. Symbols, experimental data; line, the function $\mu_0 H_C = 0.91 \text{ T} \times [1 - (T/225 \text{ K})^{1/2}]$.

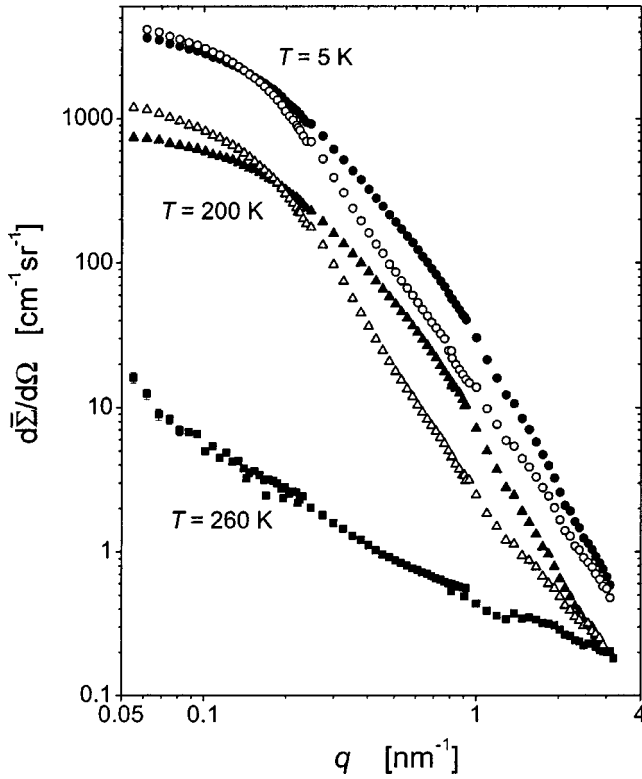


FIG. 8. Experimental differential scattering cross section $d\bar{\Sigma}/d\Omega$ versus modulus q of the scattering vector at various temperatures as indicated in the figure. Closed symbols, magnetic field $H=0$; open symbols, $\mu_0 H=4.5$ T.

Figure 7 shows the coercive field H_C as a function of the temperature. At $T=1.6$ K, the values of $\mu_0 H_C$ of cg and nc Tb are 18 and 860 mT, respectively; in other words, the reduction of the grain size results in an increase of H_C by a factor of almost 50. By inspection of the figure it is seen that the data for nc Tb can be well fitted by $H_C \propto 1 - (T/T_0)^{1/2}$. The result for the characteristic temperature, $T_0=225$ K, agrees well with the temperature of the maximum of the ac susceptibility, $T=224$ K, and with the paramagnetic Curie temperature, $\theta_p=226$ K, deduced from fits to the paramagnetic ac susceptibility of nc Tb.

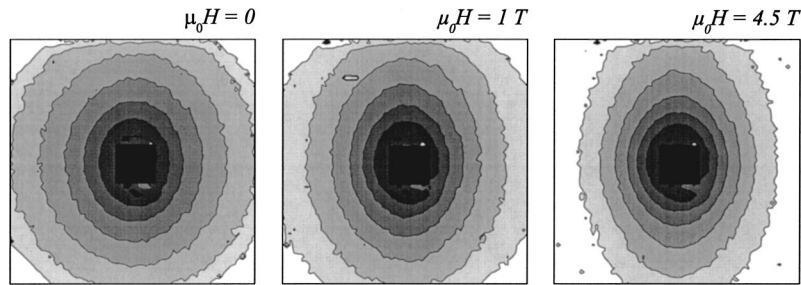


FIG. 9. Gray-scale coded map of the experimental scattering intensity recorded on the two-dimensional position-sensitive detector at temperature $T=5$ K and at three different magnetic fields as indicated in the figure. The field direction is vertical, and the maximum value of the magnitude q of the scattering vector (measured from the center of the square horizontally to an edge) is 0.92 nm $^{-1}$. Subsequent shadings denote doubling of the intensity, with darker regions corresponding to higher intensity. The central black squares mask the region of the beam stop.

D. SANS

Figure 8 shows the radial average differential scattering cross section $d\bar{\Sigma}/d\Omega$ at different applied magnetic fields and temperatures. It is seen that at all fields the scattering cross section in the ferromagnetic state is considerably higher than that in the paramagnetic state. This suggests that the former is dominated by the spin-misalignment scattering, whereas the nuclear contribution is small. It is also seen that the effect of increasing H_a on the scattering cross section of ferromagnetic Tb is dramatically different from the case of soft magnets, where applied fields of 2 T have been found to align the magnetization with the field direction, thereby reducing the magnetic scattering by several orders of magnitude.^{11,13} By comparison, $d\bar{\Sigma}/d\Omega$ in Tb is seen to depend only weakly on H_a , indicating that the maximum applied field of 4.5 T is insufficient to align the spins along the field direction. What is more, the scattering curves exhibit a crossover at about $q=0.2$ nm $^{-1}$; in other words, increasing H_a has the counter-intuitive effect of increasing the scattering contrast at small q .

The conjecture that the scattering in the ferromagnetic state is dominated by the spin-misalignment scattering is supported by inspection of the variation of the total differential scattering cross section (prior to removal of the residual scattering) as a function of the azimuthal angle ϑ (the angle between \mathbf{q} and the applied field \mathbf{H}_a) on the detector (see Fig. 9). As can be seen in the figure, the scattering cross section is largest in the direction parallel to the applied magnetic field. This finding confirms qualitatively the $(1 + \cos^2 \vartheta)$ law of spin-misalignment scattering, as opposed to the $\sin^2 \vartheta$ variation expected for residual scattering, and it emphasizes that a separation of magnetic and nuclear scattering based on a $\sin^2 \vartheta$ law would fail for the present samples.

Figure 10 displays the nuclear interference function $P_{\text{nuc}}(q)$ computed from the SANS data by means of Eq. (11). By combining $P_{\text{nuc}}(q)$ with Eq. (12), using experimental magnetization data for $\langle M \rangle$, we have determined the spin-misalignment scattering $d\bar{\Sigma}_M/d\Omega$ in the ferromagnetic state, which can be inserted into Eq. (9) to obtain the expectation value of the magnitude square of the Fourier components of the magnetization, per volume. The results for m^2/V are shown in Fig. 11. Figure 12 displays correlation functions

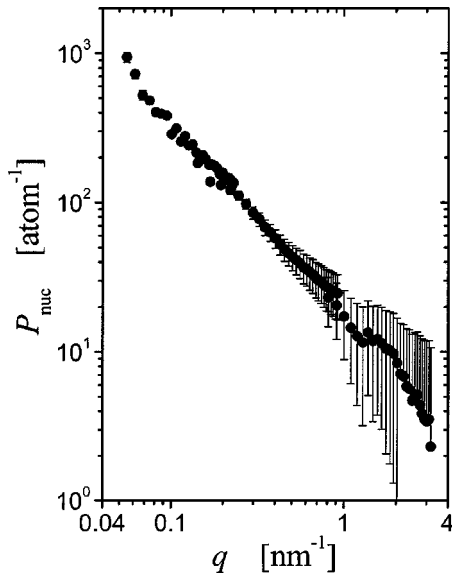


FIG. 10. Experimental nuclear interference function P_{nuc} versus the modulus q of the scattering vector.

computed from this data via Eq. (18). Data are only shown for $r \geq 2$ nm, in accordance with the limited experimental resolution (compare Sec. II C).

The correlation is seen to be significantly field dependent. At interatomic distances less than 8 and 5 nm at 5 and 200 K, respectively, $C(r)$ decays as a function of increasing H_a . Beyond these interatomic spacings, $C(r)$ reflects the opposite behavior: the highest applied field is associated with the largest values for $C(r)$. In the limit of interatomic distances much larger than the grain size, $C(r)$ becomes nearly independent of the applied field. The graphs of $C(r)$ at all fields and temperatures could be fitted excellently by parabolas in the interval $2 \leq r \leq 3.5$ nm, and these fits were used to estimate the value C_0 of the correlation function at $r=0$ by extrapolation. Figure 13 shows the reduction of the net magnetization due to the spin-misalignment fluctuations, computed from the experimental C_0 and Eq. (22). At $T=5$ K the results agree with magnetometer data, especially for the remanent state. This supports the validity of our SANS data

analysis, and it indicates that the reduced remanence at small grain size (compare Sec. IV C above) can be ascribed entirely to the spin misalignment on the nanometer length scale which is probed by SANS. Any contributions of a conceivable macroscopic domain structure can only be relatively minor.

The good agreement of the magnetization inferred from SANS with the magnetometer data at $T=5$ K contrasts with the results for $T=200$ K. At the higher temperature, the Fourier components of the spin misalignment are smaller than at $T=5$ K, which indicates a more ordered spin arrangement and less reduction of the magnetization due to static spin misalignment, whereas the overall magnetization is considerably decreased. The apparent disagreement is readily understood in terms of the different response of the experimental techniques to thermal excitation of the spin system: magnetometry is equally sensitive to the reduction of the net magnetization by static as well as dynamic (thermal) disorder of the spin system, whereas SANS may or may not detect spin waves, depending on the dispersion relation and on the neutron wavelength. Since the SANS experiment does not discriminate between elastic and inelastic scattering, the spin dynamics may enter the data through magnon scattering. However, as was argued in Sec. II B, the large energy gap in the dispersion relation of Tb prohibits inelastic scattering at the wavelength used in our experiment. This suggests that the SANS data of the present work are exclusively due to the static spin structure, and that the effect of the spin dynamics at higher T , which is responsible for the reduced macroscopic magnetization, is not included in the experimental $C(r)$.

In Fig. 14 the negative inverse logarithmic derivative of the correlation function is plotted versus r . Linear extrapolation to $r \rightarrow 0$ supplies the characteristic length l_C of the spin misalignment defined in Sec. II C. The results are shown in Fig. 15. It is seen that, at $T=5$ K, l_C exhibits a weak minimum as a function of the field, the values varying between 1.5 and 2 nm, close to the experimental resolution of roughly 2 nm. This indicates that, at $T=5$ K, the disorder in the spin system is dominated by structure on the scale of 2 nm or less, throughout the entire range of applied fields in our experi-

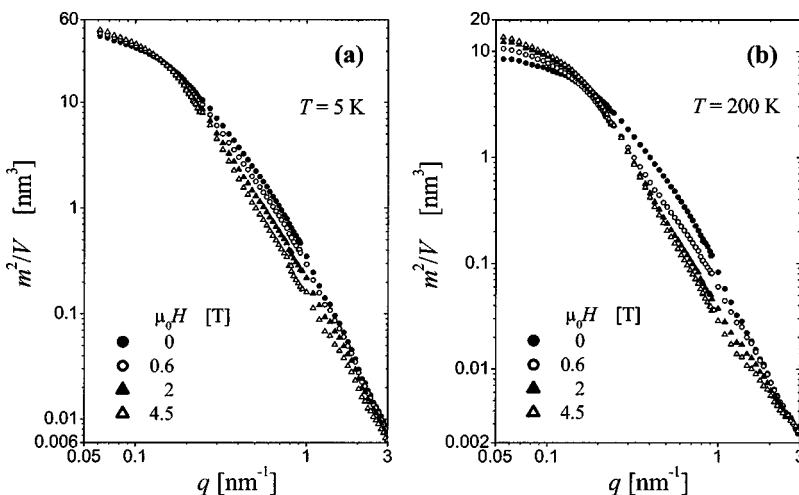


FIG. 11. Magnitude square of the Fourier coefficients (per volume) of the magnetization versus modulus q of the scattering vector at temperature $T=5$ (a) and 200 (b) K at various applied magnetic fields as indicated in the figure.

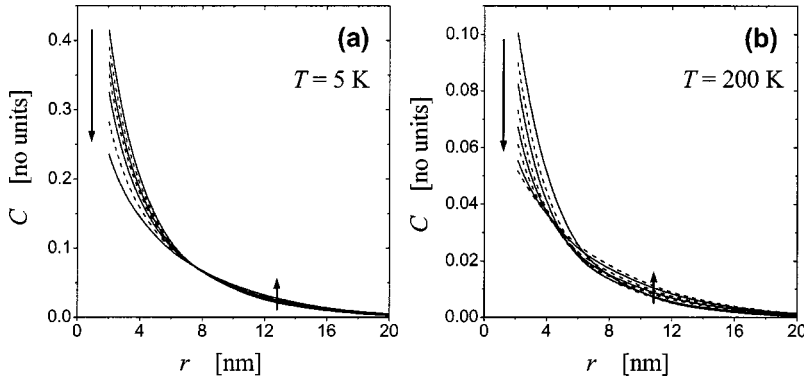


FIG. 12. Correlation function $C(r)$ at temperature $T=5$ (a) and 200 (b) K. Magnetic fields (in order of decreasing C at small r): (a) $\mu_0 H_a = 0, 0.2, 0.4, 0.6, 1, 2,$ and 4.5 T; (b) $\mu_0 H_a = 0, 0.1, 0.2, 0.4, 0.6, 1, 2,$ and 4.5 T. Down and up arrows denote the trend of the variation of C at small and medium r , respectively, when H is increased. Data are shown only for $r > 2$ nm, to account for the limited resolution of the scattering data.

ment. Since this scale is smaller than the grain size of 9 nm, the scattering must arise from internal nonuniformity of the magnetization *within* the individual nanograins.

At 200 K Fig. 15 shows that l_C exhibits a stronger variation as a function of the field: after an initial drop l_C increases from its minimum value of less than 2 nm to about 5 nm at $\mu_0 H_a = 4.5$ T. The finding of an initial drop of l_C as H_a is increased is in qualitative agreement with what is derived theoretically by analysis of the magnetic interactions in soft magnets,¹⁷ and confirmed by experiment in nc Ni and Co:⁴² the effect of the applied field is to selectively suppress the Fourier components \mathbf{m} with the longest wavelengths, so that progressively smaller structures survive as the field is increased. However, as compared to the soft magnets at similar values of H_a , the characteristic lengths in Tb are found more than one order of magnitude smaller. What is more, the characteristic length in Tb (at least at $T=200$ K) increases when the field is increased above about $\mu_0 H_a = 1$ T. An explanation of this finding will be given in Sec. V B below.

V. DISCUSSION

A. Implications of magnetization data and correlation functions

The magnetization data of our experiments show, as the most obvious effect of reducing the grain size of Tb to the nanometer scale, a significant reduction of the magnetization at all fields and temperatures investigated. It is noteworthy that the finding of a reduced remanence in the nc material, relative to cg Tb, is in contradiction to the general trend of an *enhanced* remanence in nanocrystalline hard magnets,^{43,44}

which constitutes one of the reasons for the commercial interest in these materials for application as hard magnets. A conceivable explanation would be a reduction of the mean magnetic moment at grain boundaries. *Ab initio* computations for grain boundaries in Ni suggest a small reduction in the moment,⁴⁵ and some experimental studies of nc transition metals report a more dramatic decrease.⁴⁶ However, the more recent experimental studies have found practically no size dependence of the saturation magnetization in nc Ni and nc Co;¹⁴ in fact it was convincingly demonstrated that the previously reported size dependence in transition metals is an artifact due to impurities.⁴⁷ In the present study the analysis of the paramagnetic susceptibility data shows that the mean atomic magnetic moment is unaffected by the grain size, so that the reduction of the magnetization cannot be the result of a possible reduction in the moment at grain boundaries. This is in agreement with the expectation that, due to the localized nature of the $4f$ electrons, which are responsible for the magnetism in Tb, the atomic magnetic moment should depend only weakly on the atomic short-range order.

The analysis of the correlation functions has led us to the conclusion that the spin orientation varies considerably on length scales smaller than the grain size. In other words, and in agreement with the conclusions drawn from the susceptibility data, the reduced magnetization is not due to a reduction of the atomic magnetic moment, but results from the internal spin disorder in the grains. The agreement of the magnetization computed from SANS with that measured by magnetometry shows that, at low T , this intragrain spin disorder involves fluctuations of the spin orientation of sufficient magnitude to account for the entire field dependence of

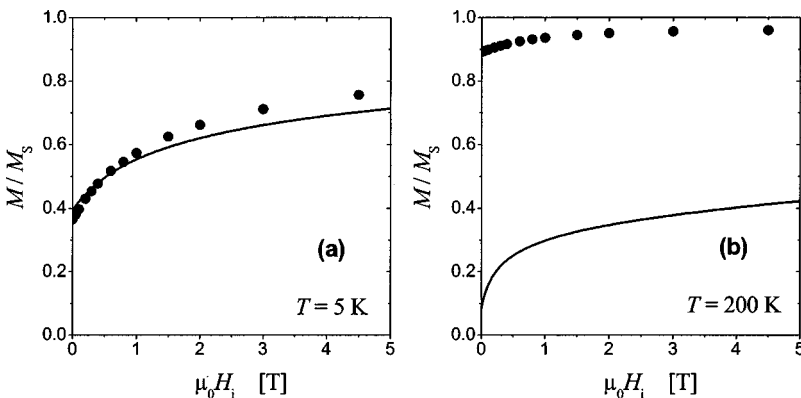


FIG. 13. Reduced magnetization M/M_S (using $M_S = 328$ A m²/kg) versus internal magnetic field H_i at temperatures $T=5$ (a) and 200 (b) K. Solid lines, magnetometer data; circles, estimated from the extrapolated value of the spin-misalignment correlation function at $r=0$ via Eq. (22).

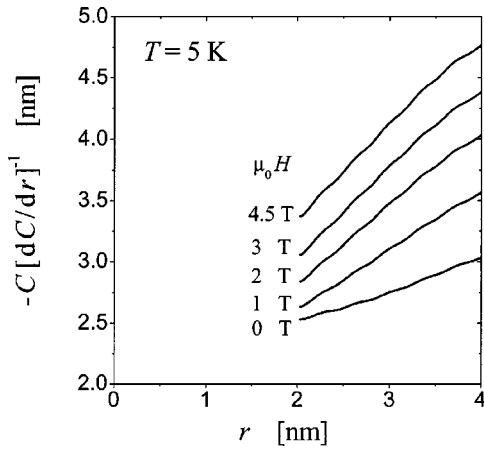


FIG. 14. The negative inverse of the logarithmic derivative of the correlation function $-[d \ln(C)/dr]^{-1}$ versus the interatomic distance r for the data in Fig. 12(a). The characteristic length l_C was determined by linear extrapolation of this function to $r=0$.

the magnetization, and for a reduction of the net magnetization by more than 50% of M_S in the remanent state. It is emphasized that the reduced remanence due to intragrain spin disorder, which reduces the net magnetization of each grain, is quite different from the demagnetization of a conventional coarse-grained ferromagnet, which occurs by the formation of macroscopic domains with inverse magnetization. A gradual formation of domains *within* the individual nanograins, which would be required to explain the continuous variation of C_0 and l_C as a function of the field, is not compatible with the large coercive force of nc Tb.

In Tb, the “easy axes” of the magnetization are in the basal plane of the hexagonal crystal lattice. The strength with which the anisotropy counteracts the canting of the moments out of the plane is measured by the magnitude of a fictitious magnetic field which acts in the plane and tends to align the moments with the plane.⁴⁸ For an anisotropy energy density $V_{20}P_2[\cos(\theta)]$, where V_{20} and P_2 denote the second Legendre polynomial and the associated anisotropy coefficient,

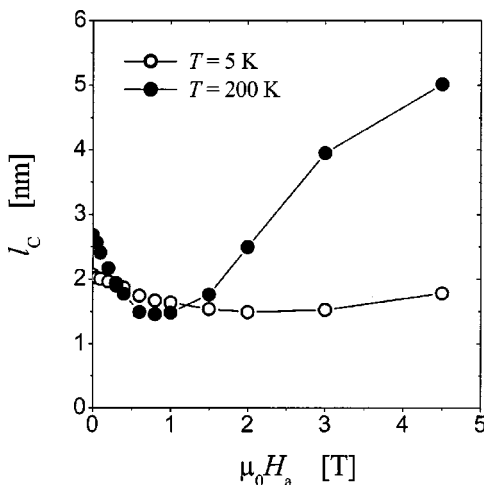


FIG. 15. Characteristic length l_C versus applied field H_a at temperatures $T=5$ and 200 K, as indicated in the figure.

the magnitude of the field is $3V_{20}/(\mu_0\langle M \rangle)$. With the experimental value^{48,49} $V_{20}=5.65 \times 10^7$ J/m³, the estimated field has the very high value of 62 T at $T=5$ K. At 200 K, where V_{20} is decreased to 1.1×10^7 J/m³, and $\langle M \rangle$ is reduced to $0.6M_S$,⁵⁰ one still obtains a large value, 20 T. The maximum experimental field in the SANS experiment had the much smaller value of 4.5 T, it was therefore insufficient to cant the moments significantly. Therefore, it is concluded that under all experimental conditions the net magnetization of each crystallite remained essentially locked in to the local hexagonal basal plane, and that the intragrain spin disorder involves variations of the orientation of the moments in the basal planes.

It is tempting to identify the torque on the moments in the grain boundary regions—which arises from the exchange interaction with the neighboring grains of different crystallographic orientation—as the reason for the intragrain spin misalignment. However, this cannot be the dominant effect in nc Tb, since we observed a decreased remanent magnetization, whereas it is known that the exchange interaction will on average enhance the remanence in fine-grained hard magnets, as mentioned above. Thus, it appears that the intragrain spin disorder must result from the two remaining fields that give rise to a torque on the moments which is nonuniform within each grain: the magnetostatic stray field from the neighboring grains, and/or the magnetoelastic anisotropy due to nonuniform microstrain and stress within the nanograins.

In view of the absence of a grain-size dependence of the atomic magnetic moment, the decreased paramagnetic susceptibility must be understood as an effect of modified magnetic interaction. Since there is also little size dependence of θ_P , the most obvious explanation is in terms of the anisotropy energy: In Tb single crystals the paramagnetic susceptibility is reduced along the axis of high anisotropy energy in the ferromagnetic state, the c axis. By analogy, the finding of a reduced paramagnetic susceptibility in nc Tb suggests that on average the anisotropy energy in the nc material is higher than that of the annealed sample. Conceivably, this extra anisotropy originates from magnetoelastic effects related to the microstrain in nanocrystalline materials.

As a matter of fact, the above contention is much in evidence at the common observation of enhanced microstrain in nc metals, typically on the order of several tenths of a percent—a value within the uncertainty of our x-ray data. Microstrain is a result of elastic interactions of varying sign and magnitude at the boundaries to the various grains.⁵¹ It is manifest as interplanar as well as in-plane interatomic distance fluctuations which are nonuniform within the individual crystallites. Therefore, it seems plausible to assume that magnetoelastic anisotropy forces the orientation of the anisotropy field to vary nonuniformly within each grain. The microstrain is not resolved by the diffraction data, but a lower bound is provided by the intrinsic microstrain, which is required to achieve a close packing of randomly oriented crystalline grains when the discrete nature of the crystal lattice precludes continuous adjustment of the dimensions without strain.⁵¹ For fcc metals this implies $\langle \varepsilon^2 \rangle^{1/2} \approx (0.05 \text{ nm})/D$, and a roughly similar value would be expected for hcp due to the essentially similar interplanar spac-

ings. This suggests a comparatively large rms strain, of the order of 0.5% in nc Tb. Since Tb exhibits a large magnetostriction, in particular when the magnetization is rotated within the basal plane,⁵² a considerable strain-induced in-plane magnetic anisotropy is expected to result from the microstrain.

The finding of a suppression of the antiferromagnetic state in nc Tb is consistent with the notion of a nonuniform magnetoelastic anisotropy. The dependency of antiferromagnetic order on the grain size has previously been investigated for nc Cr,^{53,54} and a similar suppression of the ordering transition was found when the material was prepared by inert-gas condensation.⁵³ The finding has been argued to be in agreement with the notions that (i) the order is suppressed when the size of the magnetic unit cell (9–10 lattice constants in Tb) is comparable to the grain size and (ii) antiferromagnetic order is readily suppressed by nonuniform strain, especially in materials with a large magnetostriction, as in Tb.

Within the notion of spin disorder due to nonuniform magnetoelastic anisotropy, the finding of a lesser static disorder at $T=200$ K compared to 5 K (compare Fig. 13) can be readily understood in terms of the considerable reduction, with increasing temperature, of the in-plane magnetostriction coefficients.⁵² As a consequence, the disordering effect of the induced magnetoelastic anisotropy is reduced at the higher T , so that the spins are more efficiently aligned by the exchange interaction and by the applied field. A more detailed discussion of the q -dependent scattering cross section and of its manifestations in Figs. 11, 12, and 15 will be given in the next section.

It would be of interest to relate the temperature dependence of the coercive field to that of the magnetic anisotropy. Some nucleation models predict $H_C \propto K/\langle M \rangle$ where K is the anisotropy energy coefficient representing the dominant type of anisotropy, either magnetocrystalline or magnetoelastic.⁵⁵ Between 1.6 and 200 K the experimental coercivity in nc Tb decreases by a factor of about 17, from 860 to about 50 mT (compare Fig. 7). In the same temperature interval, as indicated above, the saturation magnetization in Tb single crystals decreases by about 40%,⁵⁰ the magnetocrystalline basal-plane anisotropy coefficient decreases by a factor of 5,^{48,49} and the magnetostriction coefficients decrease by a factor of less than 10.⁵² Consequently, the nucleation models mentioned above predict a decrease of H_C by about a factor of 6 or less, considerably less than the experimental variation in both samples, coarse grained and nanocrystalline. What is more, the temperature dependence of H_C in nc Tb is strongest as T approaches zero, whereas $\langle M \rangle$ as well as the coefficients of the magnetocrystalline anisotropy and of the magnetostriction in Tb exhibit only a weak temperature dependence for T below about 40 K. Hence, the variation of H_C is not readily explained as a consequence of the temperature dependence of the anisotropy coefficients. The $T^{1/2}$ law, which we found to provide a good empirical representation of the data for nc Tb, is characteristic for the thermally activated magnetization reversal of isolated small particles.⁵⁶ This would not be expected to be the dominant mechanism in exchange-coupled grains as in our dense, polycrystalline samples. Indeed, time-dependent measurements (to be re-

ported separately) do not support thermally activated magnetization reversal. Thus, the origin of the strong temperature dependence of H_C remains unresolved.

B. Modeling magnetic SANS

It would be desirable to predict the field-dependent SANS by nanocrystalline hard magnets based on micromagnetics models, analogous to the approach which has been applied successfully to soft magnets. Of particular interest is the explanation of the crossover of the field-dependent scattering curves and of the unusual increase of the scattering intensity at small q when the field is increased. However, in view of the nonlinear nature of the equations, the task of finding the closed-form solutions for the equations of micromagnetics, which are the basis for the analysis of scattering by soft magnets, becomes vastly more challenging when large spin misalignment needs to be admitted in plausible models for hard magnets. In fact, published micromagnetics studies of nc hard magnets have been limited to finite element numerical computations.

Since they involve a substantial numeric effort, finite element approaches do not lend themselves for routine combination with experimental SANS studies. Rather than analyzing magnetic interaction, we shall therefore restrict our considerations to a highly simplified model for the scattering which incorporates in a heuristic way what we propose to be the two most essential features of the spin structure of nc Tb: (i) the net magnetization of each grain is essentially confined to the easy plane, up to the highest fields available in our SANS study, and (ii) within the easy planes the spin system is progressively disordered as the applied field is decreased.

To this end, we analyzed the idealized limiting case where the moments have only one degree of freedom, the rotation about the axis normal to the local easy plane. When substantial simplifications are accepted, then a traceable approximate solution for the field-dependent scattering can be derived which allows to verify that the signal from this highly simplified model exhibits qualitative features in agreement with the experiment, most noticeably the crossover of the scattering curves at small q . We present this computation as supporting online material,⁵⁷ emphasizing that the nature of the assumptions is such that the model will be poorly suited for obtaining further, quantitative information on the magnetic microstructure and magnetic interactions. Nevertheless, as can be seen by inspection of the computed scattering curves (see the example in Fig. 16), the model may serve as a qualitative verification of the assumptions.

The considerations in the supporting online material⁵⁷ suggest the following explanation for the crossover of the scattering curves: at high q , $d\Sigma/d\Omega$ is dominated by the scattering of the magnetic nonuniformity on a small scale, the internal spin disorder of the individual grains. With increasing applied field, $d\Sigma/d\Omega$ is diminished as the increasing projected field within the easy planes suppresses the spin disorder and aligns the spins more in parallel within the local easy planes. At the same time, this process increases the magnitude of the net moment of each grain, while leaving its misalignment relative to the field direction constant, since all

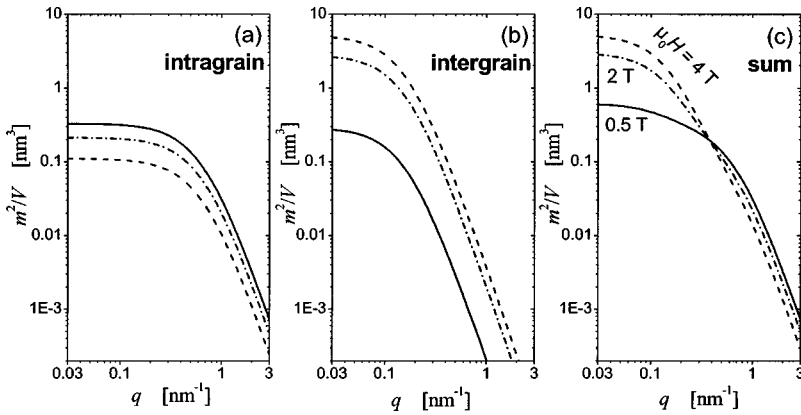


FIG. 16. Computed values of the Fourier coefficients of an idealized hard magnet at three different values of the magnetic field, as indicated in the figure. The square magnitude of the Fourier coefficients (per volume) of the magnetization versus modulus q of the scattering vector for (a) the intragrain component, (b) the intergrain component, and (c) the sum of intra- and intergrain components, which determines the experimental scattering signal. As can be seen in (c), the model reproduces the crossover of the intensity curves at low q which is observed experimentally. See supporting online material for details (Ref. 57).

moments remain locked in the respective easy planes. Since $d\Sigma/d\Omega$ at small q is dominated by the scattering contrast of structures on a scale of the grain size or larger, the field dependence will here be opposite to what is observed at high q , that is, the scattering will increase with increasing field.

Besides reproducing in a qualitative way the field dependence of the scattering cross section, the model also supplies a field-dependent evolution of the characteristic lengths in agreement with the experiment: at small H_a the largest Fourier components of the magnetization are due to the internal disorder of the spin system within each individual grain, which is characterized by a small l_C . As the field is increased this disorder is suppressed, in such a way that the Fourier components with the largest wavevector are diminished first, so that l_C is decreasing. This trend is apparent in the experimental data (compare Fig. 15). As the field is increased further the trend will continue but, eventually, the amplitude of the static fluctuations of the spin orientation within the grains becomes so small that their contribution to the overall correlation function is no longer resolved. One can then understand the experimental result for l_C by considering the magnetization within each individual grain as approximately uniform, so that the dominant nonuniformity in the spin system is due to the jump in the orientation of the net moments from grain to grain. The characteristic length representing this structure is comparable to the grain size. This means that, as the field is increased, there is a transition from a small l_C , representative of structure in the interior of the grains, to a larger l_C , representing the grain structure. The transition is not due to a single characteristic length changing its magnitude, but due to the amplitude associated with the smaller-scale structure fading, so that the contribution of the larger structure to the correlation function becomes dominant.

In support of the picture suggested above it is noted that the correlation length of idealized, spherical grains of size D is $l_C = 2D/3$ (compare Sec. II C), which yields $l_C = 6$ nm for the experimental grain size, 9 nm, of the nanocrystalline sample investigated here. Indeed, as can be seen by inspection of Fig. 15, the experimental l_C approaches this value at large applied field for $T = 200$ K. The failure to observe an analogous behavior at 5 K is consistent with fact that, due to the larger anisotropy energy, much larger applied fields, in

excess of those available in our study, are required to suppress the internal spin disorder at the lower temperature.

VI. SUMMARY

In summary, we have investigated nanocrystalline Tb with a grain size of 9 nm. The paramagnetic susceptibility data gave no evidence for a decrease of the atomic moment compared to coarse-grained Tb, but in the ferromagnetic regime we found a large increase of the coercive field. The small-angle neutron scattering signal was found to be dominated by magnetic scattering even at fields of several tesla. We have shown how the scattering due to the spin misalignment can be separated from scattering due to inhomogeneity in the atomic density, in spite of the failure of the $\sin^2 \vartheta$ law of magnetic scattering. The SANS data indicate that the magnetization remains locked in to the local basal plane of each crystallite up to fields of 4.5 T and temperatures of 200 K. This suggests, as an explanation for the large coercive field, the fact that domain wall motion is hindered at boundaries between grains with noncoplanar basal planes.

The unusual crossover of the field-dependent differential scattering cross sections, and the unusually small remanence, can be explained in terms of significant disorder of the spin system within each grain. This finding, along with the reduced paramagnetic susceptibility and the known fact that Tb exhibits large magnetostriction coefficients, indicates that nonuniform strain fields—which are unanimously reported for nanocrystalline metals, and which may even be intrinsic at small grain size—induce a magnetoelastic anisotropy which varies within each grain and which is comparable in magnitude to the in-plane anisotropy of Tb. An analysis of the correlation function of the spin misalignment indicates small characteristic length for the disorder of the spin misalignment, in agreement with the small magnetic exchange lengths of Tb and with the above-mentioned notion of small-scale spin disorder.

ACKNOWLEDGMENT

Support by the Deutsche Forschungsgemeinschaft (Heisenberg program and SFB 277) is gratefully acknowledged.

- *Corresponding author. FAX: +49 7247 82 6368. Email address: Joerg.Weissmueller@int.fzk.de
- ¹T. Schrefl, J. Fidler, and H. Kronmüller, Phys. Rev. B **49**, 6100 (1994).
 - ²R. Fischer and H. Kronmüller, Phys. Rev. B **54**, 7284 (1996).
 - ³R. Fischer, T. Leineweber, and H. Kronmüller, Phys. Rev. B **57**, 10 723 (1998).
 - ⁴M. Bachmann, R. Fischer, and H. Kronmüller, in *Magnetic Anisotropy and Coercivity in Rare-Earth Transition Metal Alloys*, edited by L. Schultz and K.-H. Müller (Werkstoff-Informationsgesellschaft, Frankfurt, 1998), pp. 217–236; H. Fukunaga and Y. Kanai, *ibid.*, pp. 237–250; W. Rave, *ibid.*, pp. 259–266; J. Fidler and T. Schrefl, *ibid.*, pp. 267–276.
 - ⁵J. Kohlbrecher, A. Wiedenmann, and H. Wollenberger, Z. Phys. B: Condens. Matter **104**, 1 (1997).
 - ⁶A. Danzig, A. Wiedenmann, and N. Mattern, J. Phys.: Condens. Matter **10**, 5267 (1998).
 - ⁷H. Hermann, A. Heinemann, N. Mattern, and A. Wiedenmann, Europhys. Lett. **51**, 127 (2000).
 - ⁸A. Heinemann, H. Hermann, A. Wiedenmann, N. Mattern, and K. Wetzig, J. Appl. Crystallogr. **33**, 1386 (2000).
 - ⁹A. Bracchi, K. Samwer, S. Schneider, and J. F. Löffler, Appl. Phys. Lett. **82**, 721 (2003).
 - ¹⁰W. Wagner, A. Wiedenmann, W. Petry, A. Geibel, and H. Gleiter, J. Mater. Res. **6**, 2305 (1991).
 - ¹¹J. Weissmüller, R. D. McMichael, J. G. Barker, H. Brown, U. Erb, and R. D. Shull, in *Nanophase and Nanocomposite Materials II*, edited by S. Komarneni, J. C. Parker, and H. J. Wollenberger, Mater. Res. Soc. Symp. Proc. No. 457 (Materials Research Society, Pittsburgh, 1997), p. 231.
 - ¹²J. Löffler, G. Kostorz, A. Wiedenmann, and W. Wagner, Physica B **241**, 603 (1998).
 - ¹³A. Michels, J. Weissmüller, A. Wiedenmann, and J. G. Barker, J. Appl. Phys. **87**, 5953 (2000); A. Michels, J. Weissmüller, A. Wiedenmann, J. S. Pedersen, and J. G. Barker, Philos. Mag. Lett. **80**, 785 (2000).
 - ¹⁴J. Weissmüller, A. Michels, J. G. Barker, A. Wiedenmann, U. Erb, and R. D. Shull, Phys. Rev. B **63**, 214414 (2001).
 - ¹⁵R. Przenioslo, R. Winter, H. Natter, M. Schmelzer, R. Hemplemann, and W. Wagner, Phys. Rev. B **63**, 054408 (2001).
 - ¹⁶A. Michels, R. N. Viswanath, and J. Weissmüller, Europhys. Lett. **64**, 43 (2003).
 - ¹⁷J. Weissmüller, R. D. McMichael, A. Michels, and R. D. Shull, J. Res. Natl. Inst. Stand. Technol. **104**, 261 (1999).
 - ¹⁸A. Michels, J. Weissmüller, and R. Birringer, Eur. Phys. J. B **29**, 533 (2002).
 - ¹⁹R. D. Greenough and N. F. Hettiarachchi, J. Magn. Magn. Mater. **31-34**, 1055 (1983).
 - ²⁰W. C. Koehler, J. Appl. Phys. **36**, 1078 (1965).
 - ²¹J. F. Löffler, H. B. Braun, and W. Wagner, Phys. Rev. Lett. **85**, 1990 (2000).
 - ²²J. Weissmüller and A. Michels, Phys. Rev. Lett. **87**, 149701 (2001).
 - ²³F. Hellman, A. L. Shapiro, E. N. Abarra, R. A. Robinson, R. P. Hjelm, P. A. Seeger, J. J. Rhyne, and J. I. Suzuki, Phys. Rev. B **59**, 11 408 (1999).
 - ²⁴R. M. Moon, T. Riste, and W. C. Koehler, Phys. Rev. **181**, 920 (1969).
 - ²⁵O. Halpern and M. H. Johnson, Phys. Rev. **55**, 898 (1939).
 - ²⁶In order to comply with our previous notation in Ref. 14 we prefer the notation of Ref. 25 over that of Ref. 24, and display results in terms of \mathbf{Q} , rather than its negative, $\mathbf{S}\perp$.
 - ²⁷G. E. Bacon, *Neutron Diffraction* (Clarendon, Oxford, 1955), Chaps. 6.2–6.3.
 - ²⁸K. Knopf and W. Waschkowski, Z. Phys. A **357**, 297 (1997).
 - ²⁹H. B. Moller and J. C. G. Houmann, Phys. Rev. Lett. **16**, 737 (1966).
 - ³⁰H. Kronmüller, in *Moderne Probleme der Metallphysik*, Vol. 2, edited by A. Seeger (Springer, Berlin, 1966), pp. 24–156.
 - ³¹A. R. Mackintosh and H. B. Moller, in *Magnetic Properties of Rare-Earth Metals*, edited by R. J. Elliott (Plenum, London, 1972), Chap. 5. The gap energy at $T=200$ K was estimated by extrapolation from the experimental interval 4–150 K to 200 K.
 - ³²J. Löffler and J. Weissmüller, Phys. Rev. B **52**, 7076 (1995).
 - ³³G. Porod, in *Small-Angle X-ray Scattering*, edited by O. Glatter and O. Krattky (Academic, London, 1982), pp. 17–51.
 - ³⁴H. P. Klug and L. E. Alexander, *X-Ray Diffraction Procedures* (Wiley, New York, 1974).
 - ³⁵D. Michels, C. E. Krill, and R. Birringer, J. Magn. Magn. Mater. **250**, 203 (2002).
 - ³⁶A. del Moral and E. W. Lee, J. Phys. F: Met. Phys. **4**, 280 (1974).
 - ³⁷D. E. Hegland, S. Legvold, and S. H. Spedding, Phys. Rev. **131**, 158 (1963).
 - ³⁸N. Schlorke, J. Weissmüller, W. Dickenscheid, and H. Gleiter, Nanostruct. Mater. **6**, 593 (1995).
 - ³⁹E. C. Stoner and E. P. Wohlfarth, Philos. Trans. R. Soc. London, Ser. A **240**, 599 (1948).
 - ⁴⁰R. W. McCallum, A. M. Cadin, G. B. Clemente, and J. E. Keem, J. Appl. Phys. **61**, 3577 (1987).
 - ⁴¹Stoner and Wolfarth (Ref. 39) have derived the remanence of an array of particles with a random orientation and with an isotropic minimum energy for the magnetization in the plane normal to a hard axis; the remanent magnetization is then $M_R = \pi M_S/4$. For a hexagonal lattice with six easy axes in the plane, there is a further reduction due to the fact that the closest easy axis deviates (by a maximum angle of $\pi/6$) from the projected field direction in the plane. This reduces the remanence by an extra factor of $3/\pi$, so that $M_R = (3/4)M_S$.
 - ⁴²A. Michels, J. Weissmüller, U. Erb, and J. G. Barker, Phys. Status Solidi A **189**, 509 (2002).
 - ⁴³N. C. Koon and B. N. Das, Appl. Phys. Lett. **39**, 840 (1981).
 - ⁴⁴J. J. Croat, IEEE Trans. Magn. **18**, 1442 (1982).
 - ⁴⁵B. Szpunar, U. Erb, G. Palumbo, K. T. Aust, and L. J. Lewis, Phys. Rev. B **53**, 5547 (1996).
 - ⁴⁶R. Z. Valiev, G. F. Korznikova, Kh. Ya. Mulyukov, R. S. Mishra, and A. K. Mukherjee, Philos. Mag. B **75**, 803 (1997).
 - ⁴⁷M. J. Aus, B. Szpunar, A. M. El-Sherik, U. Erb, G. Palumbo, and K. T. Aust, Scr. Metall. Mater. **27**, 1639 (1992); H. Kisker, T. Gessmann, R. Würschum, H. Kronmüller, and H.-E. Schäfer, Nanostruct. Mater. **6**, 925 (1995).
 - ⁴⁸S. Chikazumi, *Physics of Ferromagnetism*, 2nd ed. (Clarendon, Oxford, 1997), Chap. 12.
 - ⁴⁹S. Chikazumi, S. Tanuma, I. Oguro, F. Ono, and K. Tajima, IEEE Trans. Magn. **5**, 265 (1965).
 - ⁵⁰M. S. S. Brooks, D. A. Goodings, and H. I. Ralph, J. Phys. C **1**, 1596 (1968).
 - ⁵¹J. Weissmüller, in *Science of Metastable and Nanocrystalline Alloys*, edited by A. R. Dinesen, M. Eldrup, D. Juul Jensen, S.

- Linderoth, T. B. Pedersen, N. H. Pryds, A. Schrøder Pedersen, and J. A. Wert (Risø National Laboratory, Roskilde, Denmark, 2001), pp. 155–176; <http://www.risoe.dk/afm/symp22>
- ⁵²J. J. Rhyne and S. Legvold, *Phys. Rev.* **138**, A507 (1965).
- ⁵³M. R. Fitzsimmons, J. A. Eastman, R. A. Robinson, A. C. Lawson, and J. D. Thompson, *Phys. Rev. B* **48**, 8245 (1993); M. R. Fitzsimmons, J. A. Eastman, R. B. Von Dreele, and L. J. Thompson, *ibid.* **50**, 5600 (1994).
- ⁵⁴R. Przenioslo, I. Sosnowska, G. Rousse, and R. Hempelmann, *Phys. Rev. B* **66**, 014404 (2002).
- ⁵⁵A. Aharoni, *Introduction to the Theory of Ferromagnetism*, 2nd ed. (Clarendon, Oxford, 1996).
- ⁵⁶B. D. Cullity, *Introduction to Magnetic Materials* (Addison-Wesley, Reading, MA, 1972), Sec. 11.6.
- ⁵⁷See EPAPS Document No. E-PRBMDO-69-090401 for derivation of the magnetic small-angle neutron scattering of an idealized hard magnet. A direct link to this document may be found in the online article's HTML reference section. The document may also be reached via the EPAPS homepage (<http://www.aip.org/pubserve/epaps.html>) or from <ftp.aip.org> in the directory /epaps/. See the EPAPS homepage for more information.